Supplementary Information: Real time optical observation and control of atomically thin metal chalcogenide synthesis

Hamid Reza Rasouli[1], Naveed Mehmood[1], Onur Çakıroğlu[2], T. Serkan Kasırga[1,2]*

[1] UNAM – Institute of Materials Science and Nanotechnology, Bilkent University, Ankara 06800, Turkey

[2] Department of Physics, Bilkent University, Ankara 06800, Turkey

* Corresponding Author: kasirga@unam.bilkent.edu.tr

Table of Contents

1. Supplementary Movies
2. CVD Chamber
   2.1. Alumina heaters
   2.2. Auxiliary components
   2.3. Thermal simulations
3. Characterization of a typical WSe_2 crystal
4. Early stage of NaCl – WO_3 reaction
5. Formation of sodium tungsten bronze with H_2
6. Characterization of a typical $MoSe_2$ crystal
7. Heterostructures

Supplementary Text

1. Supplementary Movies

Figure S1. The video shows the formation of WSe_2 atomically thin layers via vapor-solid-solid and vapor-liquid-solid growth routes.

Figure S2. Reaction between NaCl and WO_3 mixture in real time.

2. CVD Chamber

The chamber is composed of 3 main parts: (1) cooling base, (2) reactor, (3) lid. Cooling base holds the main cooling channels for the reactor. Reactor is the housing that has the hermetically sealed electrical feedthroughs and the gas inlet and outlets. The lid is also composed of 3 main parts. The lid body, sapphire window and sapphire window holder is assembled in a vacuum tight way. The cooling channels within the lid helps to keep the lid cool. All the body parts are machined out of 6061 Aluminium alloy as it offers 10 times higher thermal conductivity compared to 304 stainless steel. Images of the setup is given in **Figure S3**.

2.1. Alumina Heaters

We cast alumina heaters, using a mixture of 85% Al_2O_3, 5% kaolin and 10% water mixture with Kanthal A1 22 Ga wire coils placed within the mould. Then, we dry the green body at 100 °C to evaporate the excess water and mixture to set. Finally, the green body is sintered at 1400 °C for three hours. This forms a solid body, yet as the sintering temperature is kept low to prevent deterioration of Kanthal wires it is not as strong as alumina produced by other methods.

After the heaters are sintered, we place thermocouple 1 mm deep into the surface and by using a hand-held infrared thermometer we check the accuracy of the reading by the thermocouple. If the reading is accurate within ± 10 °C, we place the heater in the chamber. For the substrate heaters we perform one final calibration using NaCl. A few grains of NaCl is placed on an oxidised chip and its melting point is observed on the substrate heater. If it agrees ± 20 °C with the melting point of NaCl, we start using the heater. Typically, the heaters last for many growth cycles. Indeed, most of the studies we reported in this paper has been performed using the same set of heaters. Care must be taken especially during cooldown. Sudden changes in the heater current result in expansion and contraction of the Kanthal wire, which weakens the heater over time.

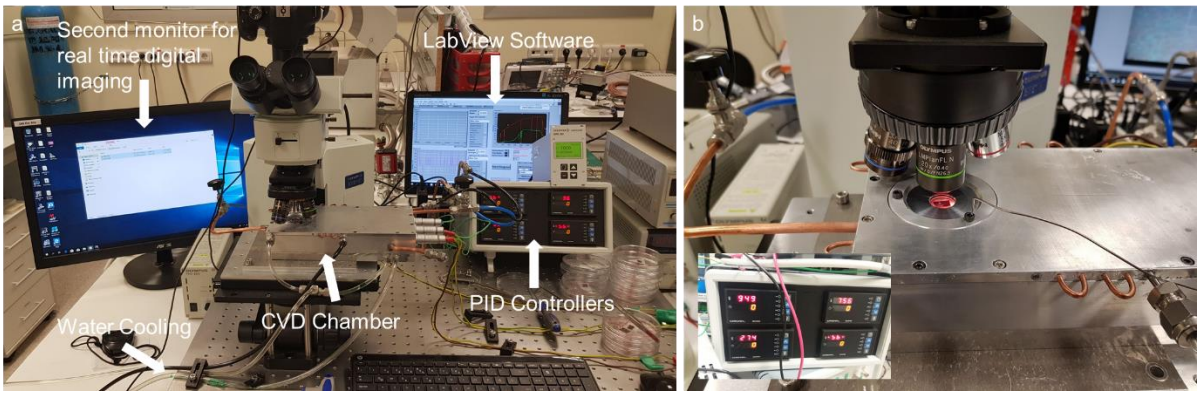

Figure S3 Pictures of the custom-made CVD setup **a,** Picture shows the layout of the overall setup. Some essential components are labelled on the picture. **b,** Close-up view of the chamber running at high temperature. Inset picture shows the PID controller assembly that indicates the temperatures of the substrate heater (top left), heater 1 (top right) and heater 2 (bottom left) during a synthesis.

2.2. Auxiliary components

Whole CVD chamber is orchestrated via a LabView program that controls the mass flow controllers and the heater temperatures. Also, we use a 700 W/h chiller to keep the chamber walls cold. Typically, we keep the coolant temperature around 10 °C. The CVD chamber is assembled on an Olympus BX 51WI fixed stage microscope. The focusing is performed via moving the nosepiece rather than the stage. For the X-Y motion, the whole chamber moves thanks to the flexible piping and cabling. The microscope is equipped with a 5x, a 20x and an ultra-long working distance 40x objective with 20x multiplication at the eyepiece. A Canon DSLR camera is connected to the microscope for capturing HD video and high-resolution pictures.

2.3. Thermal simulations

We modelled the heater configuration in an Ar atmosphere by using a finite element analysis software (COMSOL). Although we simulated by gas flow as well, since the flow rate is low it makes no difference on the temperature profile. For the analysis we kept the top lid at 50 °C and the heater at 800 °C. Thermal analysis shows that when the surface of the heater is at 800 °C, temperature within the first mm is above 600 °C. Results of the analysis are given in **Figure S4**. The thermal gradient towards the lid creates a convection current. This convection carries some of the vaporized precursors up to the lid and the observation window. For many materials we synthesized, this causes no problem while for some that has high vapor pressure, condensation of the evaporated matter on to the observation window hinders the vision.

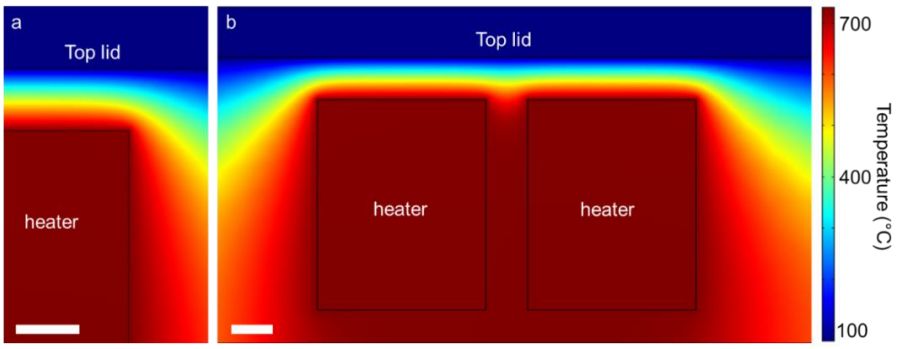

Figure S4 Cross-sectional view of the thermal distribution within the CVD chamber **a,** Single heater configuration and **b,** double heater configuration. Scale bar represents 3 mm.

3. Characterization of a typical WSe_2 crystal

Figure S5a shows an optical picture of a typical crystal synthesized in our custom CVD chamber via vapour-solid-solid route. Raman and photoluminescence (PL) intensity maps (**Figure S5b-c**) show that the crystal is uniform, and the PL spectrum is similar to that has been reported previously[1]. We also performed atomic force microscopy on our crystals to measure their thicknesses. Raman peak positions match with the ones reported in the literature (**Figure S5d**). The PL spectrum given in **Figure S5e** is fitted with two Gaussian peaks: The major peak is centred around 1.621 eV with a full-width half-maximum (FWHM) of 60 meV and the secondary peak is centred around 1.550 eV with 58 meV FWHM. The stronger peak at 1.621 eV is attributed to neutral free A-excitons while the peak at 1.550 eV is attributed to the trions. In WSe_2 mechanically cleaved from the bulk, trion peak is closer to the exciton peak in energy and the exciton peak is located around 1.658 eV. However, our measured values are very typical of CVD synthesized WSe_2 monolayers[2–4]. The relative peak shifts compared to the exfoliated samples can be explained by the stress induced on the crystals due to the thermal expansion coefficient differences between the substrate and the WSe_2 crystals. AFM measurements show that (**Figure S6**) the monolayer WSe_2 has a thickness of ~0.75 nm. It is interesting to note that the surface of the crystal is covered with small dots of unknown composition.

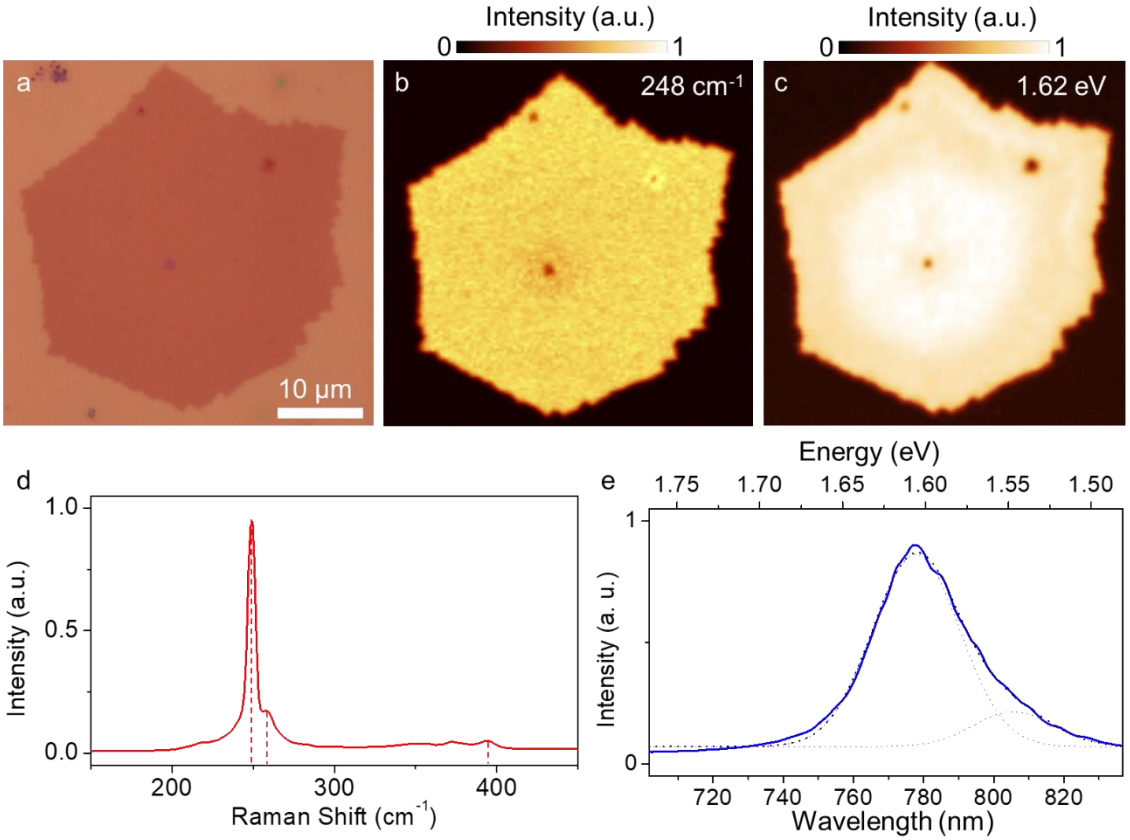

Figure S5 Characterization of a typical WSe_2 monolayer **a,** Optical microscope image of a typical crystal is given. **b,** Raman (248 cm^{-1}) and **c,** PL (1.62 eV) intensity maps show the high uniformity of the crystals. **d,** Raman spectrum taken from a point on the crystal shows the typical Raman features of the monolayer WSe_2. **e,** PL spectrum taken from a point on the crystal is similar to the previously reported CVD grown monolayers of WSe_2. Gaussian fits to the spectrum are represented by purple dotted lines and their sum is by black dotted line.

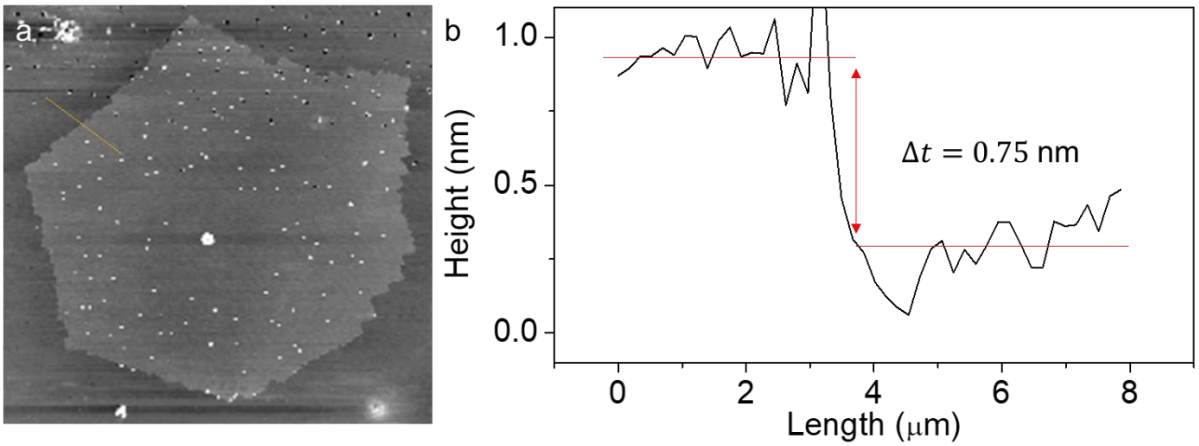

Figure S6 AFM topography of a monolayer WSe_2 **a,** AFM height map and **b**, the height trace taken along the yellow dashed line in **a** show that the apparent thickness of the crystal is 0.75 nm.

We would like to note that crystals formed via vapour-liquid-solid phase typically have much poorer crystal quality. Most often they are composed of multi-layered regions and the crystals are polycrystalline with multiple defects. **Figure S7** shows a crystal grown within HfO_2 on SiO_2 channels (50 nm deep, 5 μm wide) via directing the VLS precursor. First, the PL peak is significantly reduced and shifted to 1.568 eV. PL intensity and FWHM varies significantly across the crystal. Similarly, the Raman intensity map shows intensity variations across the crystal.

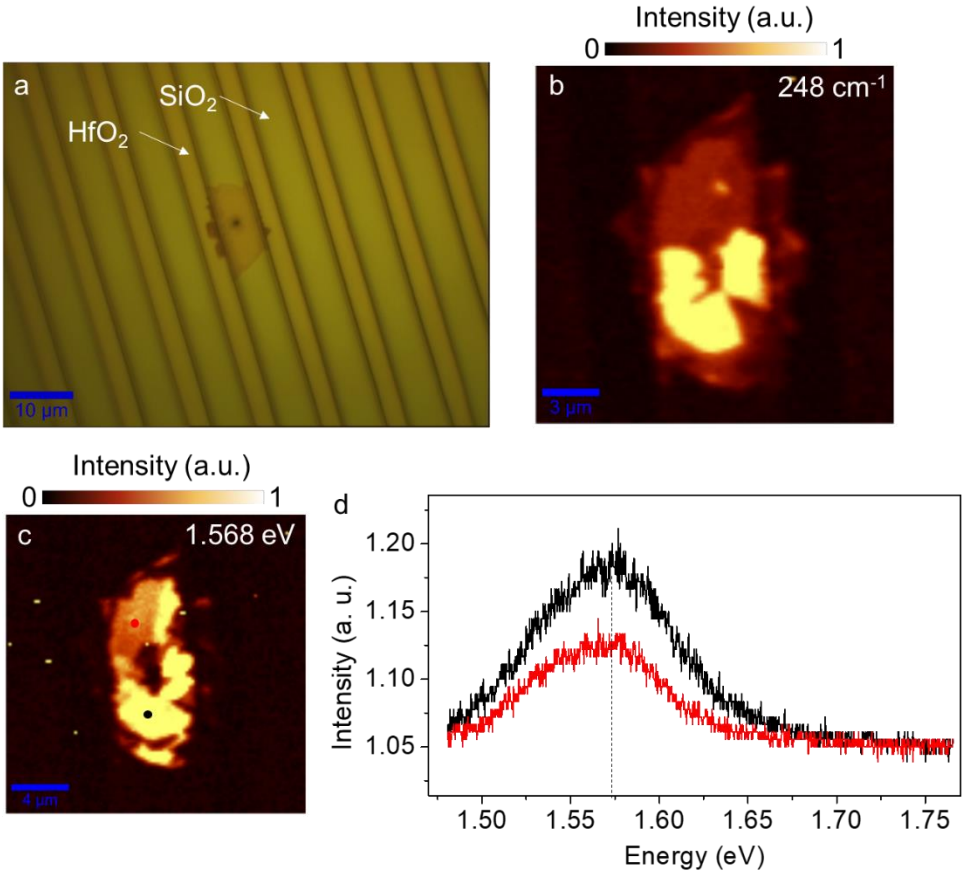

Figure S7 a, Optical microscope micrograph of a crystal formed via VLS mode within the channels formed by HfO_2 on SiO_2. **b,** Raman intensity map of 248 cm^{-1} peak shows dramatic

intensity variations across the sample. However, the peak position stays the same. **c**, PL intensity map integrated at 1.568. As comparison to VSS formed crystals, the peak position is very much shifted and the FWHM is larger. **d,** Shows the PL graphs taken from the marked locations on **c**.

4. Early stage of NaCl – WO_3 reaction

Figure S8 shows EDX analysis on a WO_3 particle at an early stage of the synthesis. EDX maps in **Figure S8 b-g** shows that Na and Cl coexist in certain locations on WO_3 grain.

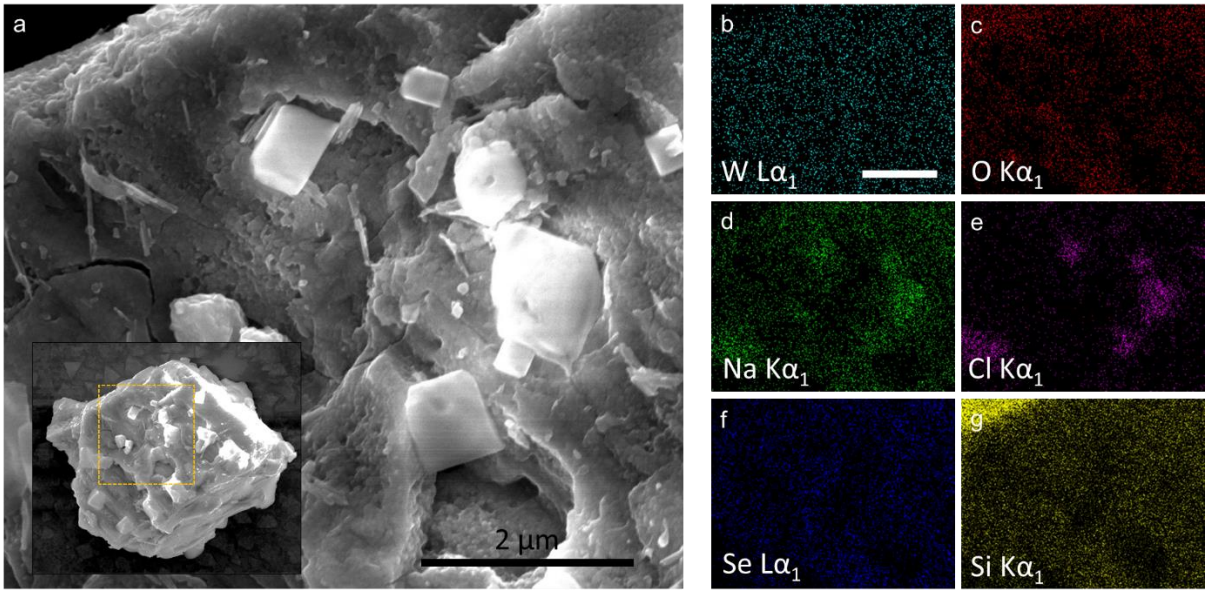

Figure S8 EDX of early stage NaCl – WO_3 reaction **a,** SEM image of a WO_3 grain shows crystal formations on the surface **b-g,** EDX maps taken from the same region shows that there are regions where NaCl particles recrystallized on the WO_3 surface. Comparing **d** and **e** reveals that not all the Na on the surface is in NaCl form. **f**, Although no Se is introduced, as the Se $L\alpha_1$ peak coincides with the tail of the W $L\alpha_1$ peak, we observe an erroneous distribution of Se all over the material.

5. Formation of Sodium Tungsten bronze with H_2

As mentioned in the main text, when we introduce hydrogen gas to Na_2WO_4, crystals of various colours ranging from yellow to grey form as shown in **Figure S9a-b**. EDX (**Figure S9c-g**) and XPS (**Figure S9h**) measurements show that these crystals are sodium tungsten bronzes which has a form of Na_xWO_3, $x < 1$. Varying colours correspond to different x.[5] W $4f$ binding energies are consistent with the sodium tungsten bronze[6] and Raman spectrum (**Figure S9i**) taken from the crystals are also consistent with the Raman spectra of alkali tungsten bronzes[7].

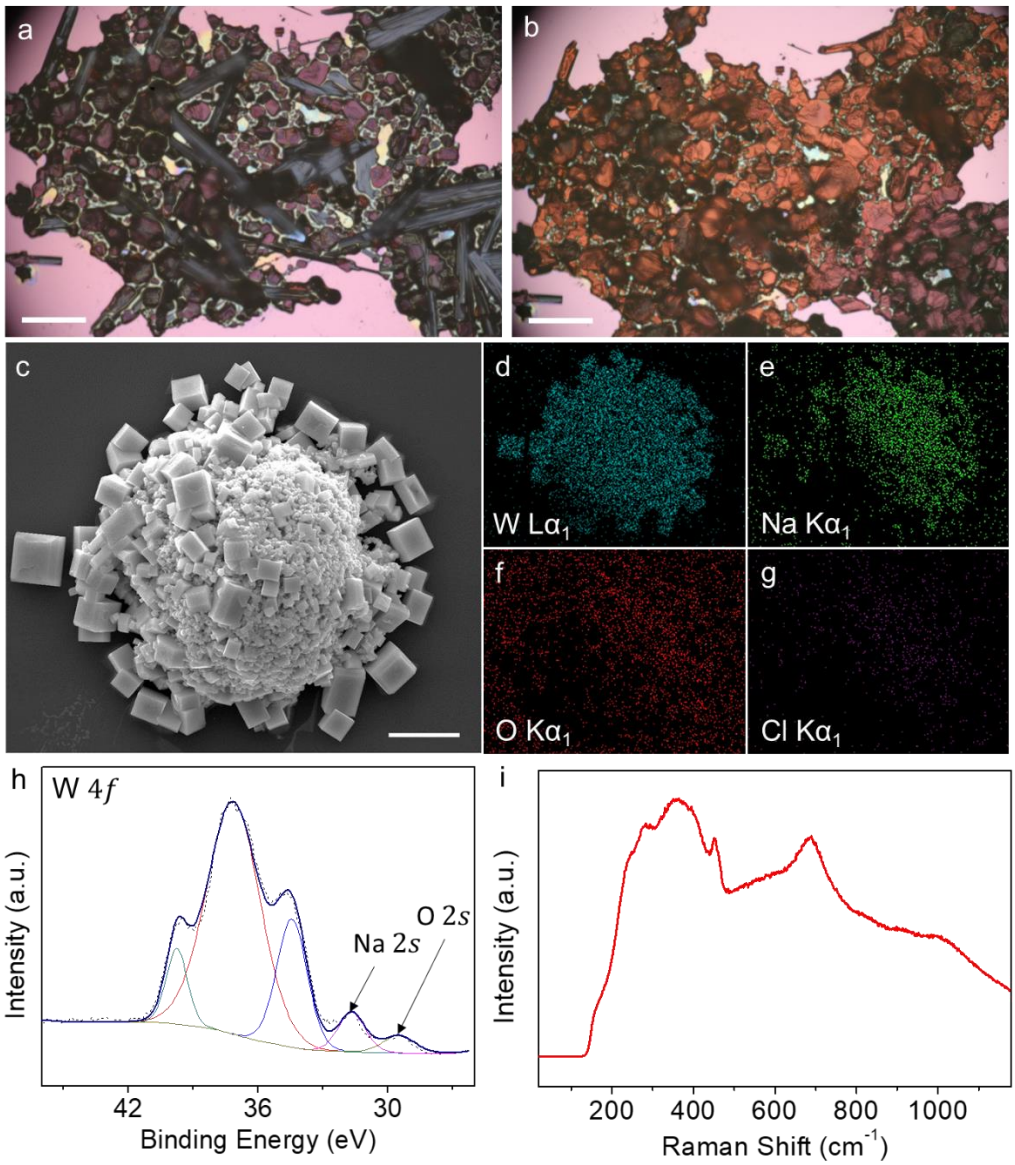

Figure S9 Sodium Tungsten bronze formation **a, b,** Optical micrographs show crystals of various colours after exposing Na_2WO_4 liquid droplet to H_2. The colours we observe in these formations are consistent with the reported colours for Na_xWO_3. Scale bars are 100 µm. **c.** SEM micrograph and **d-g** corresponding EDX maps. **h,** XPS survey of W $4f$ binding energy taken from sodium tungsten bronze formation indicates that W is in +4 oxidation state. **i,** Raman spectrum of sodium bronze.

6. Characterization of a typical $MoSe_2$ crystal

Figure S10a shows an optical picture of a typical $MoSe_2$ crystal synthesized in our custom CVD chamber. AFM measurements given in **Figure S10b** shows a monolayer thickness of 0.72 nm. Raman and photoluminescence (PL) maps (**Figure S10c-d**) show that the crystal is uniform, and the PL spectrum is similar to that has been reported previously[8,9].

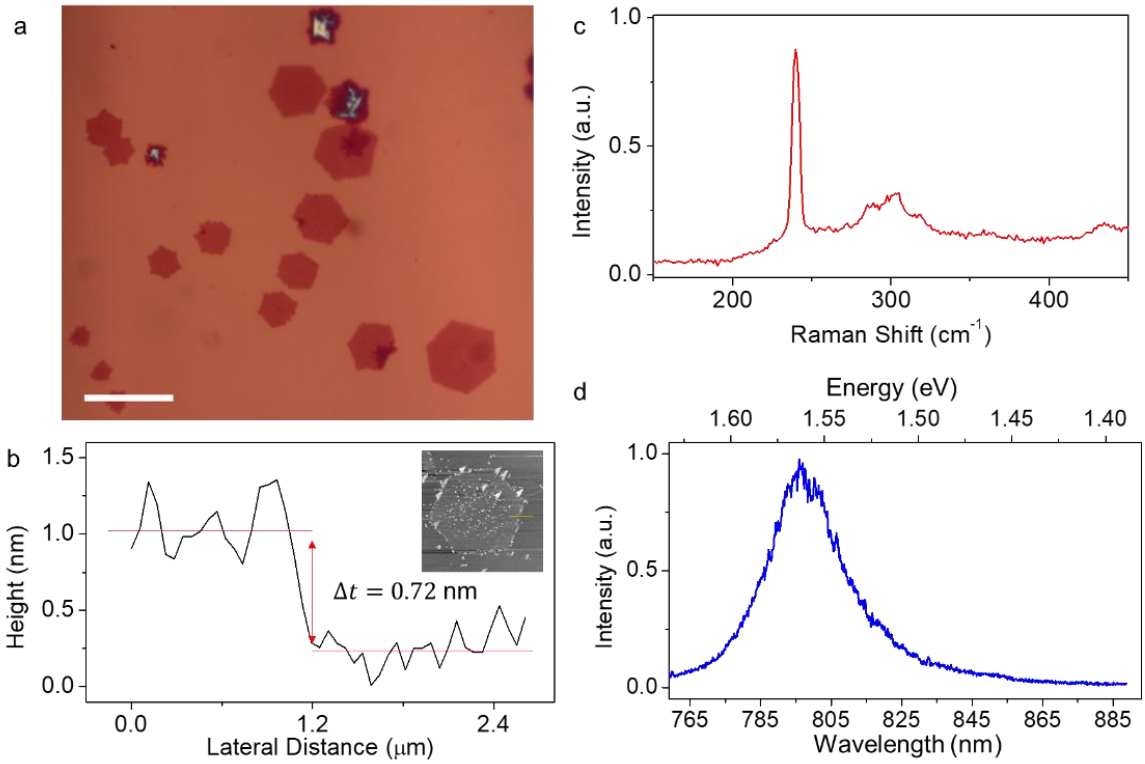

Figure S10 Characterization of a typical $MoSe_2$ crystal **a,** Optical micrographs of hexagonal $MoSe_2$ monolayers on SiO_2/Si. **b,** AFM height trace taken along the dashed line in the inset topography map shows that the average height of the crystal is 0.72 nm. **c**, Raman spectrum and **d,** photoluminescence spectrum are consistent with the CVD growth $MoSe_2$ monolayers.

7. Heterostructures

Vertical $MoSe_2$/WSe_2 heterostructure formation starts with formation of Na_2WO_4 droplet on the $MoSe_2$ crystals. We stopped the synthesis as the droplet formed and took Raman spectra to characterize its contents. As expected, the Raman spectra from the frozen droplet matches with the Na_2WO_4 as shown in **Figure S11**.

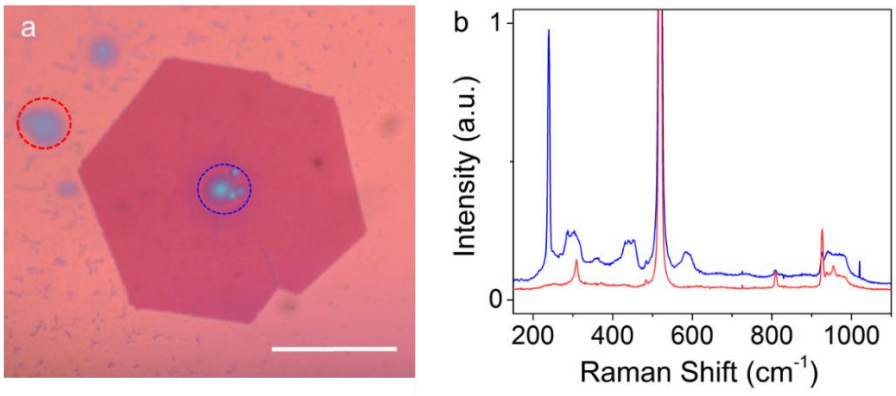

Figure S11 Vertical heterostructure formation. **a.** Optical microscope image of a Na_2WO_4 droplet on $MoSe_2$ monolayer. **b.** Raman spectra taken from the dashed circles in **a** match with the Raman spectrum of Na_2WO_4. Extra peaks in the Raman spectrum taken over the $MoSe_2$ flake is from the $MoSe_2$.

References

1 B. Liu, M. Fathi, L. Chen, A. Abbas, Y. Ma and C. Zhou, *ACS Nano*, 2015, **9**, 6119–6127.

2 J. K. Huang, J. Pu, C. L. Hsu, M. H. Chiu, Z. Y. Juang, Y. H. Chang, W. H. Chang, Y. Iwasa, T. Takenobu and L. J. Li, *ACS Nano*, 2014, **8**, 923–930.

3 S. M. Eichfeld, L. Hossain, Y.-C. Lin, A. F. Piasecki, B. Kupp, A. G. Birdwell, R. A. Burke, N. Lu, X. Peng, J. Li, A. Azcatl, S. McDonnell, R. M. Wallace, M. J. Kim, T. S. Mayer, J. M. Redwing and J. A. Robinson, *ACS Nano*, 2015, **9**, 2080–2087.

4 S. Lippert, L. M. Schneider, D. Renaud, K. N. Kang, O. Ajayi, J. Kuhnert, M.-U. Halbich, O. M. Abdulmunem, X. Lin, K. Hassoon, S. Edalati-Boostan, Y. D. Kim, W. Heimbrodt, E.-H. Yang, J. C. Hone and A. Rahimi-Iman, *2D Mater.*, 2017, **4**, 025045.

5 Y. Xue, Y. Zhang and P. Zhang, *Phys. Rev. B*, 2009, **79**, 205113.

6 J.-N. Chazalviel, M. Campagna, G. K. Wertheim and H. R. Shanks, *Phys. Rev. B*, 1977, **16**, 697–705.

7 S. Rahman, University of Bremen, 2015.

8 J. C. Shaw, H. Zhou, Y. Chen, N. O. Weiss, Y. Liu, Y. Huang and X. Duan, *Nano Res.*, 2014, **7**, 511–517.

9 Y.-H. Chang, W. Zhang, Y. Zhu, Y. Han, J. Pu, J.-K. Chang, W.-T. Hsu, J.-K. Huang, C.-L. Hsu, M.-H. Chiu, T. Takenobu, H. Li, C.-I. Wu, W.-H. Chang, A. T. S. Wee and L.-J. Li, *ACS Nano*, 2014, **8**, 8582–8590.